Korean J. Chem. Eng., 32(3), 397-405 (2015)
DOI: 10.1007/s11814-014-0229-6

pISSN: 0256-1115
eISSN: 1975-7220

A pore-scale model for the cathode electrode of a proton exchange membrane fuel cell by lattice Boltzmann method

Gholam Reza Molaeimanesh[‡] and Mohammad Hadi Akbari[†]

Center for Fuel Cell Research, School of Mechanical Engineering, Shiraz University, Shiraz 71348-51154, Iran
(*Received 17 February 2014 • accepted 10 August 2014*)

Abstract−A pore-scale model based on the lattice Boltzmann method (LBM) is proposed for the cathode electrode of a PEM fuel cell with heterogeneous and anisotropic porous gas diffusion layer (GDL) and interdigitated flow field. An active approach is implemented to model multi-component transport in GDL, which leads to enhanced accuracy, especially at higher activation over-potentials. The core of the paper is the implementation of an electrochemical reaction with an active approach in a multi-component lattice Boltzmann model for the first time. After model validation, the capability of the presented model is demonstrated through a parametric study. Effects of activation over-potential, pressure differential between inlet and outlet gas channels, land width to channel width ratio, and channel width are investigated. The results show the significant influence of GDL microstructure on the oxygen distribution and current density profile.

Keywords: Proton Exchange Membrane Fuel Cell, Lattice Boltzmann Method, Cathode Electrode, Electrochemical Reaction, Pore-scale Model

INTRODUCTION

Increased atmospheric pollution and depleting fossil fuel resources have made the search for sustainable energy sources inevitable. Hydrogen as an energy carrier is at the center of attention in this new scenario, being compatible with renewable energy sources and the preferred fuel for fuel cells. Among different types of fuel cells, the proton exchange membrane (PEM) fuel cell shows the most promising future because of its many advantages over other fuel cell types including high power density, low operating temperature, high efficiency and low emissions [1]. PEM fuel cells are being actively developed for use in cars and buses, as well as for a wide range of portable applications, and for combined heat and power (CHP) systems [2]. Nevertheless, there are still some barriers for their commercialization such as cost and durability issues which make fundamental research for their development unavoidable. The ability to model reactant gas transport along with electrochemical reactions in the electrodes is critical, particularly in the cathode where the oxygen reduction reaction (ORR) is sluggish and inefficient [3]. Many such numerical models have been proposed in the literature [4,5]. In almost all of these models the gas diffusion layer (GDL) is treated as a homogeneous and isotropic porous medium with uniform morphological properties such as porosity, tortuosity, and permeability, while GDLs are actually highly non-homogeneous and anisotropic [6,7]. Therefore, a numerical technique capable of taking into account heterogeneous and anisotropic effects is needed to reach a better prediction of cathode performance. With enhanced computational resources becoming available in recent years, the lattice Boltzmann method (LBM) has emerged as a powerful tool for modeling heterogeneous and anisotropic transport phenomena in a complicated porous medium such as GDL or catalyst layer (CL) of a PEM fuel cell at pore scale. LBM has several advantages over other conventional CFD methods in dealing with complex boundaries, in parallelization of the algorithm and in modeling multi-phase fluid flow in a porous medium [8]. Hence, modeling different types of fuel cells by LBM has been growing in the past decade [9-11].

Several LBM investigations of GDL and CL transport properties, such as permeability, have been reported [12-17]. Dynamic behavior of liquid water in the channel or GDL of a PEM fuel cell has also been modeled recently using LBM [18-23]. To the best of our knowledge, in all of previous LBM investigations the cathode electrode is not simulated completely where no electrochemical reaction is considered (with the exception of investigations by Chen et al. [21-23]). Moreover, in the only investigations where cathode is simulated with the inclusion of electrochemical reaction, i.e. [21-23], the species transport is modeled through a passive approach. This approach may lead to lack of accuracy especially when species fractions become comparable, such as at high over-potentials, and hence no component can be considered as a solvent [24]. On the other hand, an active approach in which the velocity fields of all species are solved separately can lead to more accurate results.

In the present study, a pore-scale model for species transport in the cathode GDL of a PEM fuel cell with interdigitated flow field is proposed. The core of the paper is the implementation of electrochemical reaction with an active approach in a multi-component LB model for the first time. Although the model presented here is a single phase, it has the potential to be further developed

[†]To whom correspondence should be addressed.
E-mail: h-akbari@shirazu.ac.ir
[‡]Present address: School of Automotive Engineering, Iran University of Science and Technology, Tehran, Iran

into a multi-phase model. This model allows investigating multi-component gas transport in cathode GDL taking into account electrochemical reaction on CL and considering heterogeneity and anisotropy effects of the porous GDL.

NUMERICAL APPROACH

1. LBM Framework

Unlike conventional numerical schemes based on discretization of macroscopic continuum equations, the lattice Boltzmann method is based on microscopic models and mesoscopic kinetic equations simplified for a lattice. The kinetic nature of LBM introduces some extraordinary features that distinguish it from other numerical methods such as the linearity of transport equation (in comparison with nonlinear Navier-Stokes equations), calculating pressure by an equation of state (in comparison with calculating pressure by solving Poisson differential equation), etc. [8].

The present numerical model is based on the lattice Boltzmann method with a single relaxation time collision operator (the so-called BGK model [25]) and the popular D2Q9 lattice scheme. The "2" in D2Q9 refers to the number of lattice dimensions and "9" refers to the number of possible directions for a particle movement in the lattice.

The lattice Boltzmann equation which is derived from simplification of Boltzmann equation in a lattice [26] can be expressed as:

$$f_i(\vec{r}+\vec{c}_i\Delta t,\, t+\Delta t) = f_i(\vec{r},\, t) + \frac{\Delta t}{\tau}\left[f_i^{eq}(\vec{r},\, t) - f_i(\vec{r},\, t)\right] \tag{1}$$

where f_i is the density distribution function in direction i, f_i^{eq} is the equilibrium density distribution function, $\vec{r}$ refers to space position, t is time, $\vec{c}_i$ the velocity vector in direction i, and τ the relaxation time which is related to kinematic viscosity, ν, by $\tau=1/2+3\nu$. Equilibrium density distribution function is calculated as:

$$f_i^{eq} = w_i\rho\left[1+\frac{\vec{c}_i\cdot\vec{u}}{c_s^2}+\frac{1}{2}\frac{(\vec{c}_i\cdot\vec{u})^2}{c_s^4}-\frac{1}{2}\frac{\vec{u}\cdot\vec{u}}{c_s^2}\right] \tag{2}$$

where w_i is the weighting factor, $\rho=\sum_i f_i$ is the fluid density, $\vec{u}=\sum_i f_i\vec{c}_i / \sum_i f_i$ is fluid velocity and c_s is the speed of sound in the lattice. For D2Q9 lattice scheme, $c_s=1/\sqrt{3}$ and w_i is equal to {4/9, 1/9, 1/9, 1/9, 1/9, 1/36, 1/36,1/36, 1/36} for i={0, …, 9}.

Eq. (1) is solved through collision and streaming processes which are shown for D2Q9 scheme in Eqs. (3) and (4), respectively.

$$f_i(x,\, y,\, t+\Delta t) = f_i(x,\, y,\, t)\left[1-\frac{\Delta t}{\tau}\right] + \frac{\Delta t}{\tau}f_i^{eq}(x,\, y,\, t) \tag{3}$$

$$f_i(x+\Delta x,\, y+\Delta y,\, t+\Delta t) = f_i(x,\, y,\, t+\Delta t) \tag{4}$$

To incorporate boundary conditions, f_i must be determined at the boundaries. A simple and powerful LBM boundary condition applicable for no-slip wall is called "bounce-back," which is based on the idea that particles colliding with a wall in a direction will bounce back in the opposite direction [27]. In fact, this boundary condition gives LBM the ability to model fluid flow in complicated geometries such as pore space of a porous medium. Several versions of this boundary condition have been proposed [24]; however, the half-way version in which the wall is located half-way between two neighboring grids is mostly used.

2. Simulating Multi-component, Single-phase Fluid Flow

Generally, two distinct passive and active approaches may be used to simulate multi-component single-phase fluid flows. In a passive approach the chemical species whose mass fraction is greater than the others is considered as solvent while other species are considered as solutes. Hence, the velocity field is only solved for the solvent species before advection-diffusion equation is solved for the other species. Therefore, the velocity field is dependent only on the solvent species. This may lead to lack of accuracy when species fractions are comparable and hence no component can be considered as a solvent [24].

On the other hand, in an active approach the velocity fields for all species are solved separately; this is a more realistic approach leading to more accurate results. To implement this approach in a lattice Boltzmann simulation, a multi-component multi-phase model may be adopted and by appropriate setting of model parameters the number of phases reduces to one. More clearly, the parameter which causes a phase separation in a multi-component flow is the difference between inter-particle forces acting on the particles of different components. Therefore, if these forces do not exist, no phase separation will occur and hence a multi-component single-phase flow will result. This idea of reducing the number of phases of a multi-component multi-phase model to one by omitting such forces is the basis of performing an active approach by LBM [24]. Therefore, the starting point to perform an active multi-component single-phase LB approach is selecting a multi-component multi-phase LB model.

Several multi-component multi-phase LB models have been presented in the literature. Gunstensen et al. [28] developed a multi-component LB model based on a two-component lattice gas model, which is known as the color method. Shan and Chen [29] proposed an LB model for multi-phase, multi-component fluid flows considering inter-particle interactions by a pseudo-potential function. Swift et al. [30] developed an LB multi-phase and multi-component model by using the free-energy approach. Among the aforementioned multi-phase LB models, the Shan and Chen (SC) model is widely used due to its simplicity and remarkable versatility. In the SC model, the lattice Boltzmann equation is solved for each component separately [31]; hence f_i^k will appear from now on, where the superscript k denotes the *k*th component. To incorporate multi-phase coexistence, forces are introduced to account for fluid-fluid ($\vec{F}_{coh}^{\,k}$) and fluid-solid ($\vec{F}_{adh}^{\,k}$) interactions. By choosing small or zero values for these forces the multi-component, multi-phase LB model is converted to a multi-component, single-phase LB model with active approach [24,32]. To couple lattice Boltzmann equations of different components, the composite velocity $\vec{u}'$ must be applied for all components in Eq. (2), instead of $\vec{u}^k$. The composite velocity is defined as:

$$\vec{u}' = \frac{\sum_k \frac{1}{\tau^k}\sum_i f_i^k\vec{c}_i}{\sum_k \frac{1}{\tau^k}\rho^k} \tag{5}$$

The relaxation time of each component (τ^k) is calculated through the following equation:

$$\tau^k=0.5+3\nu^k \tag{6}$$

where ν^k is the LB kinematic viscosity of component k. It is related to the physical kinematic viscosity of component k, $\nu^{k,Ph}$, through the following equation:

$$\nu^k=\nu^{k,Ph}\Delta t/\Delta x^2 \tag{7}$$

Therefore, by calculating $\nu^{k,Ph}$ at each time-step, ν^k and subsequently, τ^k can be calculated. However, to maintain the stability condition, the resulted value of τ^k must not exceed an interval.

3. Boundary Condition for a Reactive Surface

Kamali et al. [33] recently proposed a novel half-way bounce-back boundary condition for multi-component, multi-phase LBM through which surface reaction can be simulated. They showed that for a typical surface reaction A+B+…→C+E+… that is first order in A, when a particle of type A hits the wall, fraction k_{sr}^{LB} of its mass is converted into products, while the remaining fraction $(1-k_{sr}^{LB})$ is conserved as A, where:

$$k_{sr}^{LB}=\left(\frac{6k_{sr}\Delta t}{\Delta x}\right)/\left(1+\frac{k_{sr}\Delta x}{2D}\right) \tag{8}$$

and k_{sr} is the rate constant of surface reaction, Δt is time interval, Δx is the space interval in direction normal to the surface, and D is the diffusion coefficient of component A. They derived the above equation by setting equal the reaction rate in the physical framework and LBM framework. Clearly, the reaction rate in the physical framework is equal to $r=k_{sr}\rho_A(x_s)$ where $\rho_A(x_s)$ is the density of component *A* at the reactive surface. Considering the particulate nature of LBM, they demonstrated that the reaction rate in the LBM framework is equal to:

$$r=\frac{\Delta x}{6\Delta t}k_{sr}^{LB}\rho_A(x_1) \tag{9}$$

where $\rho_A(x_1)$ is the density of component *A* at the nearest fluid node to the reactive surface whose distance to the wall is $\Delta x/2$ due to applying midway bounce-back boundary condition. Although Eq. (9) was originally derived for D3Q19 lattice scheme, it can be shown that for D2Q9 scheme exactly the same equation will be obtained by applying the same derivation procedure presented in [33]. Since $\rho_A(x_1)=\rho_A(x_s)-(\Delta x/2)\nabla_x\rho_A(x_s)$ and $-D\nabla_x\rho_A(x_s)=k_{sr}\rho_A(x_s)$, one can conclude that:

$$\rho_A(x_1)=\left(1+\frac{k_{sr}\Delta x}{2D}\right)\rho_A(x_s) \tag{10}$$

Thus, Eq. (9) can be written as:

$$r=\left(1+\frac{k_{sr}\Delta x}{2D}\right)\frac{\Delta x}{6\Delta t}k_{sr}^{LB}\rho_A(x_s) \tag{11}$$

Setting Eq. (11) and $r=k_{sr}\rho_A(x_s)$ equal, Eq. (8) results. Note that to calculate k_{sr}^{LB}, all parameters on the right hand side of Eq. (8) must be in physical units.

Upon calculating k_{sr}^{LB} through Eq. (8), one can easily modify the bounce-back boundary condition to simulate a surface reaction. For instance, if a reactant particle of type A hits a reactive wall as shown in Fig. 1, its bounced back distribution function will be:

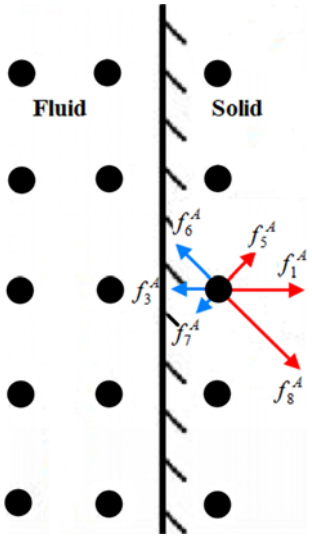

Fig. 1. Implementation of the modified bounce-back boundary condition for a reactive surface.

$$\begin{aligned} f_3^A&=(1-k_{sr}^{LB})f_1^A\\ f_6^A&=(1-k_{sr}^{LB})f_8^A\\ f_7^A&=(1-k_{sr}^{LB})f_5^A \end{aligned} \tag{12}$$

and the bounced back distribution function of a product particle of type C will be:

$$\begin{aligned} f_3^C&=\frac{MW_C}{MW_A}k_{sr}^{LB}f_1^A+f_1^C\\ f_6^C&=\frac{MW_C}{MW_A}k_{sr}^{LB}f_8^A+f_8^C\\ f_7^C&=\frac{MW_C}{MW_A}k_{sr}^{LB}f_5^A+f_5^C \end{aligned} \tag{13}$$

where MW_A and MW_C are the molar mass of A and C, respectively. Obviously, when the surface reaction is very fast ($k_{sr}\to\infty$), all the mass of a particle of type A will be consumed, and thus $\sum_i f_i^A$ will become zero. Therefore, according to Eq. (12) k_{sr}^{LB} must become equal to 2 in this case, or $\lim_{k_{sr}\to\infty} k_{sr}^{LB}=2$. As a result, in Eq. (8) must be chosen as:

$$\Delta t=\frac{\Delta x^2}{6D} \tag{14}$$

4. Validation for a First-order, Single-phase Surface Reaction

Kamali et al. [33] validated their proposed LB model by the analytical solution of a one-dimensional reaction-diffusion problem. The analytical solution of the problem they used is valid only for $Fo\ll 1$ where the Fourier number is $Fo=Dt/\ell^2$. Since in a PEM fuel cell electrode the condition $Fo\ll 1$ is not necessarily true, we have validated the model against the analytical solution of another one-dimensional reaction-diffusion problem which holds true for all Fo values. The problem is a one-dimensional diffusion in an infinite channel with two symmetric reactive surfaces, as shown in Fig. 2. Obviously, the density gradient is zero at the symmetry line (x=0). Thus, the partial differential equation will be:

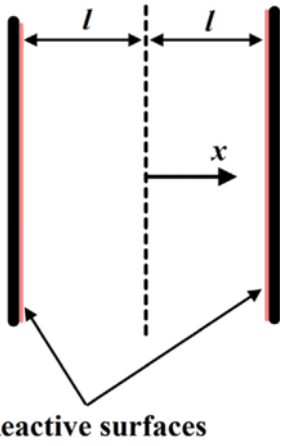

Fig. 2. Scheme of the problem used for model validation.

$$\frac{\partial \rho_A}{\partial t} = D\frac{\partial^2 \rho_A}{\partial x^2}$$
$$\rho_A(x,\, t=0) = 1$$
$$\left.\frac{\partial \rho_A}{\partial t}\right|_{x=0} = 0 \qquad (15)$$
$$\left.\frac{\partial \rho_A}{\partial t}\right|_{x=l} = -k_{sr}\rho_A(x=l)$$

where ρ_A is the density of component A. After converting to non-dimensional form and by the aid of separation of variables method, the solution will be:

$$\rho_A^*(x,\, t) = \sum_{n=1}^{\infty} \frac{4\sin(\lambda_n)}{2\lambda_n + \sin(2\lambda_n)} e^{-\lambda_n^2 Fo} \cos\left(\lambda_n \frac{x}{l}\right) \qquad (16)$$

where ρ_A^* is the non-dimensional density of component A, and λ_n s are the eigen-parameters which are the roots of equation $\lambda_n \tan(\lambda_n) = Da$, where the Damköhler number is defined as $Da = lk_s/D$. The analytical relation has been computed for the first six terms (as given in [34]) for several Da and Fo and are compared with LBM results in Fig. 3. Clearly, the LBM results are in a very good agreement with the analytical solution for all cases.

5. Electrochemical Reaction

The electrochemical reaction at the PEM fuel cell cathode electrode is the oxygen reduction reaction (ORR):

$$O_2 + 4H^+ + 4\bar{e} \leftrightarrow 2H_2O \qquad (17)$$

The rate of this reaction, r, is directly proportional to the current density, j, through r=j/4F where F is Faraday's constant. On the other hand, current density is a function of oxygen concentration (mass density divided by molar mass) and activation over-potential through Butler-Volmer equation [1]. Therefore, after some manipulation the rate equation for the electrochemical reaction on the catalyst layer (CL), which is assumed to be a thin interface, can be expressed as:

$$r = \left\{\frac{a}{4F}\left(\frac{j_{ref}}{C_{o,ref}^{\gamma_c}}\right)\left[\exp\left(\frac{\alpha_f F\eta}{R_u T}\right) - \exp\left(-\frac{\alpha_r F\eta}{R_u T}\right)\right]\right\} C_o^{\gamma_c} \qquad (18)$$

where a is the roughness factor of CL which is the ratio of CL real surface to its apparent surface, j_{ref} is the reference current density, $C_{o,ref}$ is the reference oxygen concentration on the CL, γ_c is the reduction order of ORR, α_f is the transfer coefficient for forward ORR, α_r is the transfer coefficient for reverse ORR, η is the activation over-potential and C_o is the oxygen concentration on the CL. Since γ_c=1 [1], Eq. (18) can be expressed as $r = k_{sr}C_o$ where k_{sr}, the rate

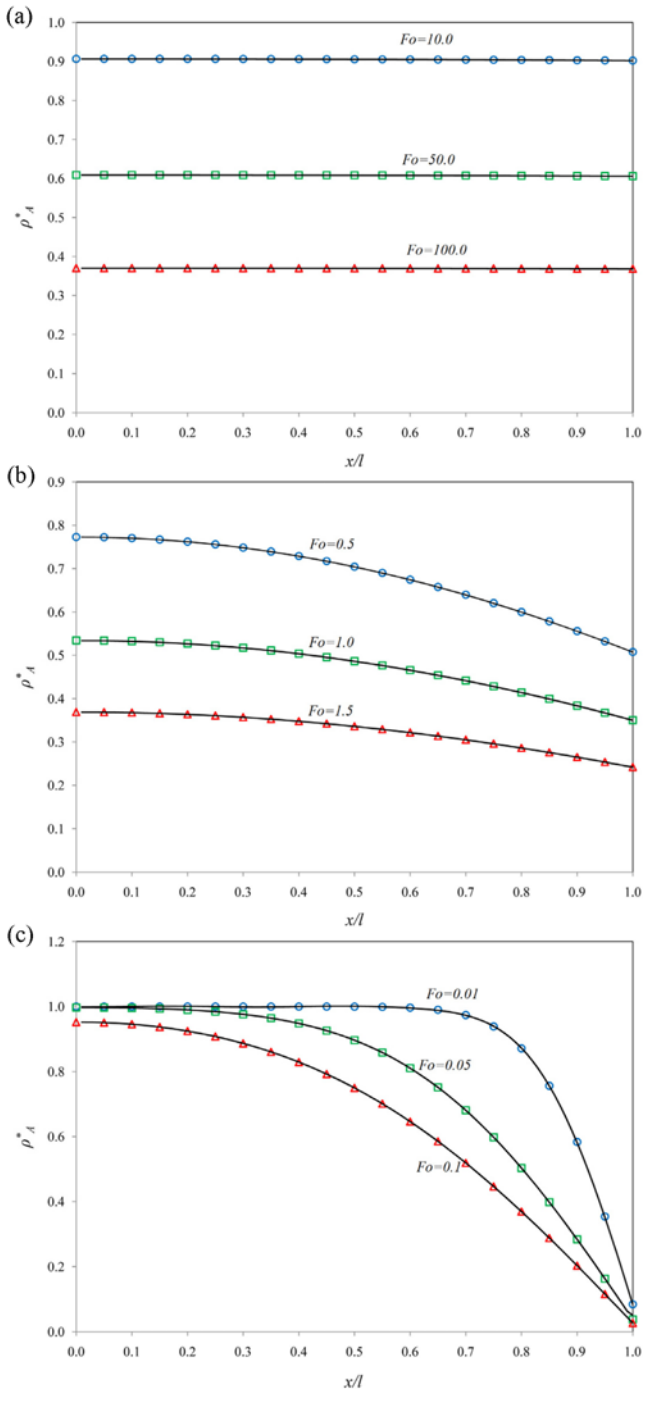

Fig. 3. Validation of the LB model by analytical solution of a diffusion problem in an infinite channel with reactive surfaces at various Fourier (Fo) and Damköhler (Da) numbers: (a) Da =0.01, (b) Da=1, (c) Da=100; symbols: LB simulation, solid lines: analytical solution.

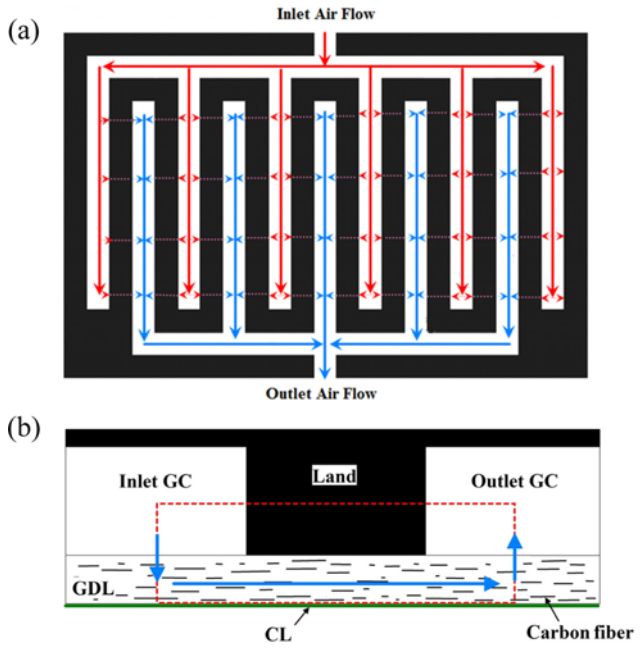

Fig. 4. A typical PEM fuel cell cathode with interdigitated flow field: (a) top view, (b) side view.

constant of the electrochemical reaction on the CL, is equal to:

$$k_{sr}=\frac{a}{4F}\left(\frac{j_{ref}}{C_{o,ref}}\right)\left[\exp\left(\frac{\alpha_f F\eta}{R_u T}\right)-\exp\left(-\frac{\alpha_r F\eta}{R_u T}\right)\right] \quad (19)$$

Upon calculating k_{sr}, k_{sr}^{LB} can be computed for the electrochemical reaction on the CL through Eq. (8) and then by applying the proposed bounce-back boundary condition, the entire cathode electrode can be simulated through an active approach.

COMPUTATIONAL DOMAIN AND BOUNDARY CONDITIONS

One of the popular and efficient flow field designs for PEM fuel cells is the interdigitated design, proposed by Nguyen [35] that has no continuous gas channels (GCs). As shown in Fig. 4(a), through a series of dead-end channel inlet fingers, air is forced into the GDL and travels under the lands into the outlet channel fingers. The dashed rectangle in Fig. 4(b) schematically shows the computational domain, which consists of half an inlet channel, half an outlet channel, as well as a land and parts of GDL and CL. The CL is simply treated as a thin interface on the bottom surface of the computational domain on which electrochemical reaction occurs. The two-dimensional GDL microstructure is adopted from Chen et al. [21]. They have shown in their investigation [21] that the transport properties of their 2D reconstructed GDL are very close to the transport properties of the real 3D GDL.

The inlet flow is considered as dry air at 1.5 atm pressure with oxygen to nitrogen molar ratio of 21/79 which reacts on the CL surface and produces water vapor. A constant pressure boundary condition is applied at the outlet, such that a constant pressure differential exists between inlet and outlet GCs. To implement the constant pressure boundary condition at the inlet and outlet, the Zou and He method [36] is used. To determine the outlet partial pressure of each component given the outlet total pressure, the mole fraction of each component at the outlet nodes is assumed equal to that at the neighboring nodes preceding the outlet. This is a valid assumption given that no electrochemical reaction occurs in the outlet channel. Knowing the outlet partial pressure of each component, the pressure boundary condition of Zou and He [36] can be applied for each species. Symmetry boundary condition is used for the left and right boundaries of the computational domain. The no-slip condition is considered on the surfaces of all solid parts. The operating condition is considered as single-phase, isothermal and steady state. All components are treated as ideal gases with different kinematic viscosities.

Table 1. Baseline simulation parameters

Parameter	Value
Operating temperature	353 K
Inlet pressure	1.5 atm
Pressure differential between inlet and outlet channels	0.01 atm
GDL thickness	200 μm
Land width	1000 μm
Channel width	1000 μm
Water vapor mole fraction in the inlet air	0.0
Oxygen mole fraction in the inlet air	0.21
Nitrogen mole fraction in the inlet air	0.79
Oxygen diffusivity in the mixture (D_O)	1.891×10^{-5} $m^2\cdot s^{-1}$ [1]
Reference oxygen concentration ($C_{o,ref}$)	10.875 $mol\cdot m^{-3}$ [1]
Roughness factor (a)	2000 [37]
Reduction order of ORR (γ_c)	1.0 [1]
Reference current density (j_{ref})	1.3874×10^{-2} $A\cdot m^{-2}$ [38]
Transfer coefficient for forward ORR (α_f)	0.5 [39]
Transfer coefficient for reverse ORR (α_r)	1 [39]

After grid independency checks, the computational domain is meshed by 1024×123 grids. A baseline simulation is first performed using a parallel FORTRAN code developed based on the proposed model. The parameter values corresponding to this baseline case are given in Table 1. Several other cases are simulated afterwards to study the impact of major contributing parameters.

RESULTS AND DISCUSSION

1. Effects of Activation Over-potential

Figs. 5 and 6 show, respectively, oxygen and water vapor mole fraction distributions for three activation over-potentials of 0.45 V, 0.5 V and 0.55 V, while other parameters are held at their baseline values given in Table 1. Moving from the inlet towards outlet gas channel (left to right), the oxygen mole fraction gradually decreases while the water vapor mole fraction gradually increases due to electrochemical reaction on the CL. As the over-potential is increased, the oxygen mole fraction decreases and the water vapor mole fraction increases due to higher electrochemical reaction rates.

It is clear in these figures that the oxygen and water vapor mole fraction distributions within the GDL are very variable and are sig-

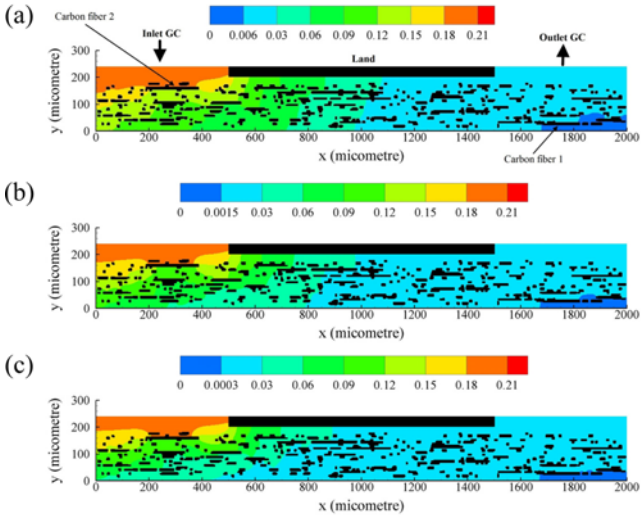

Fig. 5. Oxygen mole fraction distributions for three activation over-potentials: (a) 0.45 V, (b) 0.5 V, (c) 0.55 V.

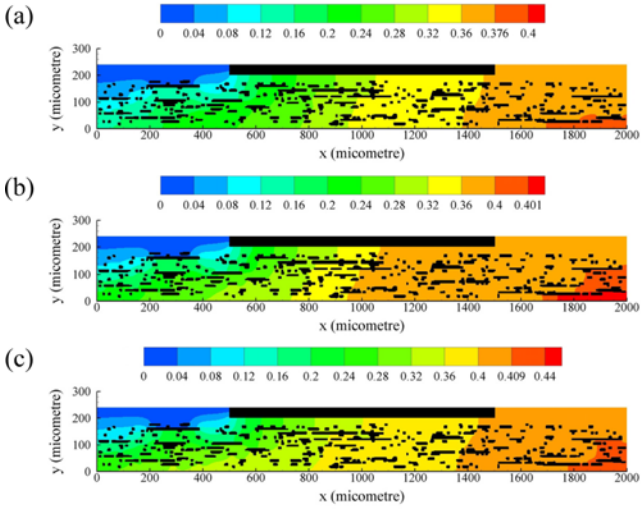

Fig. 6. Water vapor mole fraction distributions for three activation over-potentials: (a) 0.45 V, (b) 0.5 V, (c) 0.55 V.

nificantly affected by the pore structure of the GDL. In the lower-right corner of the domain under a long carbon fiber (indicated in Fig. 5(a) as carbon fiber 1) the minimal oxygen mole fraction and the maximal water vapor mole fraction appear. Oxygen starvation phenomenon is expected to initiate from this region at higher over-potentials. Since homogeneous and isotropic diffusivity of GDL has been adopted in most of the previous simulations, such predictions of possible regions in GDL for oxygen starvation are rarely reported although it can have a great influence on PEM fuel cell performance. Another long carbon fiber in the upper-left corner of the GDL (indicated as carbon fiber 2 in Fig. 5(a)) also shapes the variations of oxygen and water vapor mole fractions in that region. This carbon fiber acts as a barrier against the inlet air flow.

Fig. 7 shows the current density profiles on the CL for the three activation over-potentials; in this and similar figures l is the total length of the computational domain. Higher current density is

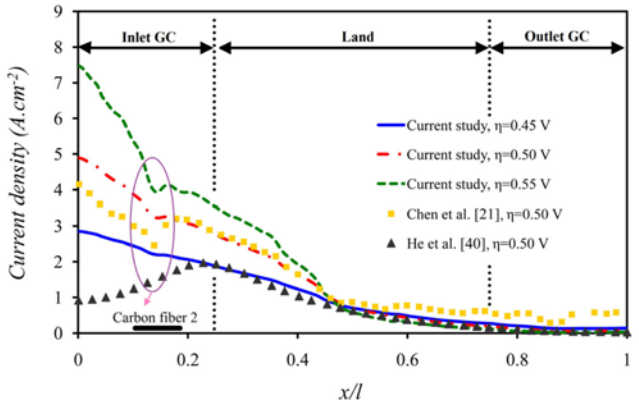

Fig. 7. Current density profiles on the catalyst layer for three activation over-potentials.

achieved at a higher activation over-potential, as predicted by the Butler-Volmer equation. In this figure, a relatively large drop is observed around x/l=0.15 due to blocking of carbon fiber 2 indicated in Fig. 5(a). Also shown in Fig. 7 are the simulation results of Chen et al. [21] and He et al. [40] for comparison.

He et al. [40] applied conventional CFD methods in their investigation; although the overall geometric dimensions are similar to our case, the GDL was modeled as a homogeneous and isotropic medium. Consequently, the current density profile was predicted relatively smooth in their simulation. In fact, in such macroscopic investigations the main parameter influencing the current density profile is the location (e.g., under channel or land) and hence such a smooth current density profile is predicted. On the other hand, in the microscopic investigations such as the present study and that by Chen et al. [21], the predicted current density profile is effectively influenced by GDL microstructure and such a smooth profile is not observed.

Chen et al. [21] used a passive LBM approach in their investigation in which nitrogen was considered as a solvent. Since water vapor and oxygen are at concentrations not much less than nitrogen concentration, their approach leads to lack of accuracy. Moreover, the inlet air velocity and operating pressure are set at 1.5 m/s and 5 atm, respectively, in [21] which are different from the present study. Therefore, in spite of the fact that the pore structure of GDL in the present study is the same as that in [21], the above-mentioned differences lead to the observed discrepancies between the predicted current density profiles. All said, a fair agreement is observed between the predicted results from the present study and those given in [21].

2. Effects of Pressure Differential between Inlet and Outlet Channels

Fig. 8 presents oxygen mole fraction distributions for four pressure differentials between inlet and outlet gas channels which are applied by maintaining the inlet pressure at 1.5 atm and adjusting the outlet pressure accordingly. The pressure differentials are 0.005 atm, 0.01 atm, 0.02 atm and 0.04 atm, while the values of other parameters are fixed as given in Table 1. It is obvious in these figures that the distribution of oxygen mole fraction is significantly affected by the pressure differential. This is because increasing the pressure

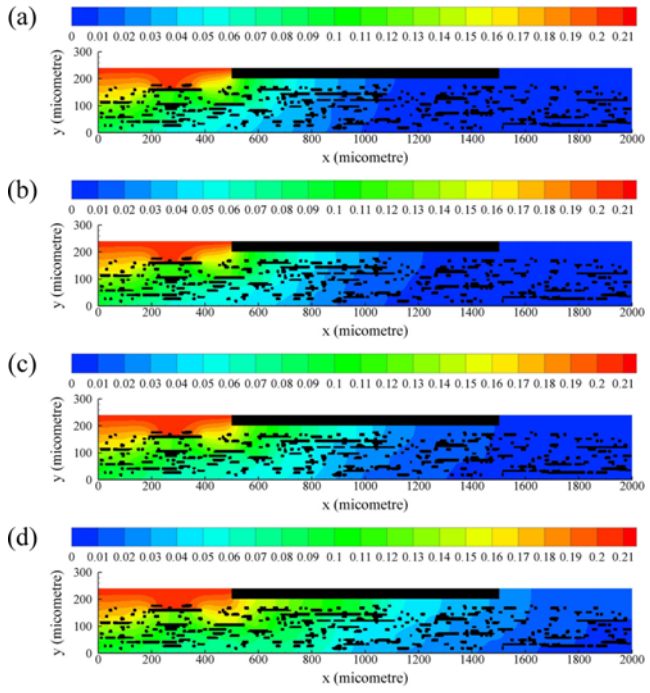

Fig. 8. Oxygen mole fraction distributions for four pressure differentials between inlet and outlet gas channels: (a) 0.005 atm, (b) 0.01 atm, (c) 0.02 atm, (d) 0.04 atm.

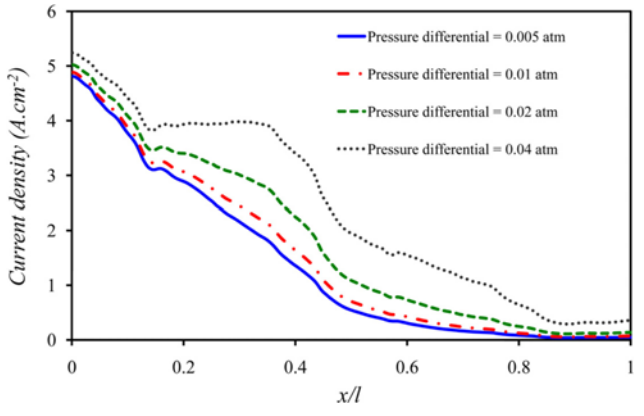

Fig. 9. Current density profiles on the catalyst layer for four pressure differentials between inlet and outlet gas channels.

differential will lead to an increased air flow rate.

Presented in Fig. 9 are current density profiles on the CL for the four pressure differentials. Higher current densities are achieved at higher pressure differentials. This is expected since increasing pressure differential leads to increased air flow rate, which in turn improves oxygen penetration through the GDL. For the highest pressure differential of 0.04 atm, the improvement of oxygen penetration through GDL is so significant that a region of almost constant current density between x/*l*=0.2 and x/*l*=0.4 is observed. This is favorable since it also leads to lower CL degradation.

3. Effects of Land Width to Channel Width Ratio

Fig. 10 shows oxygen mole fraction distributions for three ratios of land width to channel width (L/C) while the total width of the

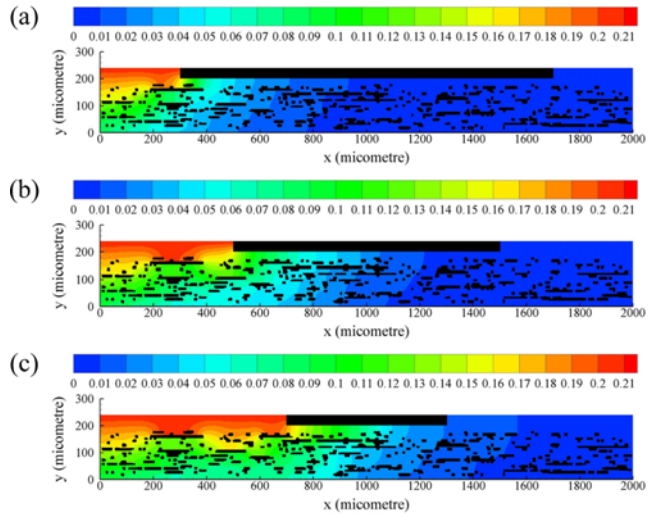

Fig. 10. Oxygen mole fraction distributions for three land width to channel width ratios: (a) L/C=1.4/0.6, (b) L/C=1.0/1.0, (c) L/C=0.6/1.4.

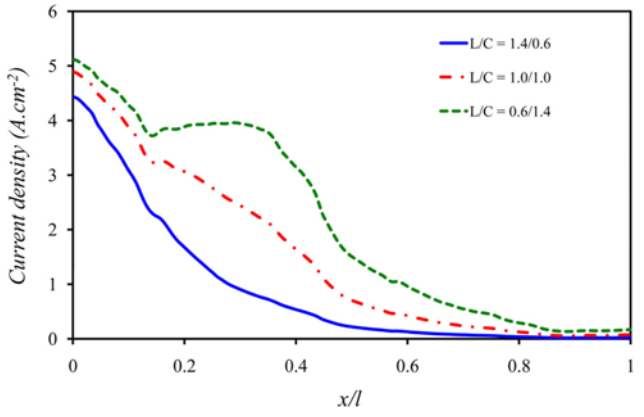

Fig. 11. Current density profiles on the catalyst layer for three land width to channel width ratios (L/C).

computational domain remains fixed at 2,000 μm. The land width to channel width ratios chosen are 1.4/0.6, 1.0/1.0 and 0.6/1.4. The values of other simulation parameters are set as given in Table 1. As L/C is decreased (while the pressure differential is fixed), the inlet air flow rate will increase due to the widening of the inlet gas channel; this in turn will improve oxygen concentration in the CL region as described previously.

Given in Fig. 11 are current density profiles on the CL for the three land width to channel width ratios. Since decreasing L/C leads to higher air flow rate, which causes higher oxygen concentration at the CL, higher current densities are expected. However, this improvement will probably be at the cost of increasing electrical resistance between the GDL and bi-polar plates. When the L/C is 0.6/1.4, the improvement of oxygen concentration at CL is so high that a region of almost constant current density between x/*l*=0.2 and x/*l*=0.4 is observed. As mentioned previously, this may lead to reduced CL degradation.

4. Effects of Channel Width

Oxygen mole fraction distributions for three channel widths of

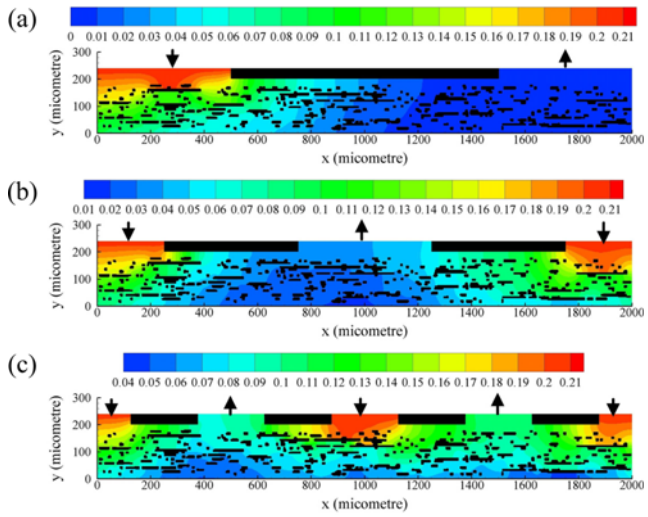

Fig. 12. Oxygen mole fraction distributions for three channel widths: (a) 1,000 μm, (b) 500 μm, (c) 250 μm; the black arrows indicate inlets or outlets.

1,000 μm, 500 μm and 250 μm are presented in Fig. 12; for these cases the ratio of land width to channel width (L/C) is 1.0/1.0, while other parameters are adjusted as shown in Table 1. Inspecting this figure shows that as the channel width is decreased (while L/C is fixed), the distribution of oxygen concentration on the CL is improved. This is caused by more uniform distribution of gas flow and enhanced penetration of air to the CL as the widths of channels and lands are reduced.

Fig. 13 shows current density profiles on the CL for these three simulation cases. It is clearly observed that as the channel (and land) widths are reduced the current density distribution is improved, i.e., higher and more uniform current density profile is observed along the CL. This uniformity in the current density also effectively lowers degradation rate of the CL. However, this enhancement will likely be at the expense of increased pressure loss along the gas channels of the cell. Obviously, for a fixed-size electrode with a given land width to channel width ratio, the number of channels will be a function of channel width. Hence, this result indicates that in such a situation a greater number of narrower channels in an interdigitated flow field will be preferred.

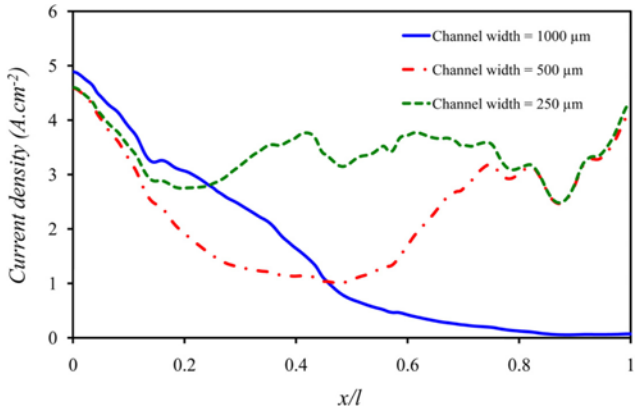

Fig. 13. Current density profiles on the catalyst layer for three channel widths.

CONCLUSIONS

A pore-scale model based on LBM is proposed for the cathode electrode of a PEM fuel cell with interdigitated flow field; heterogeneity and anisotropy effects of the GDL are included in the model. To take into account multi-component gas transport in the GDL, an active approach was incorporated in the model for the first time that enhances the accuracy especially at high activation over-potentials. The novelty of the present study is deemed as the implementation of electrochemical reaction with an active approach in a multi-component LB model. Effects of major contributing parameters were investigated, including activation over-potential, pressure differential between inlet and outlet channels, ratio of land width to channel width (L/C), as well as channel width. The results indicate that, in general, oxygen distribution and current density profile are significantly variable and are extensively affected by the pore structure of GDL. The main findings of this study are as follows:

1. The pore structure of GDL has a significant effect on the oxygen distribution; for example, if a long fiber is located near CL, it may ultimately lead to oxygen starvation at higher activation over-potentials.

2. Increasing the pressure differential between inlet and outlet channels in an interdigitated design leads to improved current densities at constant activation over-potential.

3. Decreasing land to channel width ratio (L/C) for a constant L+C value leads to higher current densities at a fixed activation over-potential.

4. Decreasing channel width when L/C=1 improves oxygen distribution on CL, hence higher and more uniform current density profiles on CL.

NOMENCLATURE

a : roughness factor
C_o : oxygen mole concentration [mol·m^{-3}]
$\vec{c}_i$: particle velocity in direction i of lattice [lu·ts^{-1}]
c_s : speed of sound in lattice [lu·ts^{-1}]
D_O : diffusion coefficient of oxygen in the mixture [m^2·s^{-1}]
Da : Damköhler number
$\vec{F}^k_{adh}$: fluid-solid interaction force acting on a particle of type k [lm·lu·ts^{-2}]
$\vec{F}^k_{coh}$: fluid-fluid interaction force acting on a particle of type k [lm·lu·ts^{-2}]
Fo : fourier number
f_i : density distribution function in direction i of lattice
f_i^{eq} : equilbrium density distribution function in direction i of lattice
f_i^k : density distribution function of component k in direction i of lattice
j : current density [A·m^{-2}]
j_{ref} : refrence current density [A·m^{-2}]
k_{sr} : rate constant of surface reaction [m·s^{-1}]
k_{sr}^{LB} : LBM rate constant of surface reaction

l : characteristic length scale [m]
MW : molar mass [kg·kmol^{-1}]
R_u : universal gas constant [J·mol^{-1}·K^{-1}]
$\vec{r}$: particle position vector [lu]
r : rate of electrochemical reaction [mol·m^{-2}·s^{-1}]
T : temperature [K]
t : time [ts]
Δt : time step [ts]
$\vec{u}$: velocity vector [lu·ts^{-1}]
$\vec{u}'$: composite velocity vector in Eq. (5) [lu·ts^{-1}]
w_i : weighting factor for direction i of lattice

Greek Symbols

α_f : transfer coefficient for forward ORR
α_r : transfer coefficient for reverse ORR
γ_c : reduction order of ORR
η : activation over-potential
λ_n : Eigen-parameter in Eq. (16)
ν : kinematic viscosity [lu^2·ts^{-1}]
ρ : density [lm·lu^{-3}]
ρ^* : dimensionless density
τ : relaxation time [ts]

Subscripts and Superscripts

A : type A species
C : type C species
f : forward reaction
i : direction i
k : component k
r : reverse reaction
ref : refrence

Abbreviations

CL : catalyst layer
GDL : gas diffusion layer
LBM : lattice boltzmann method
L/C : land width to channel width ratio
ORR : oxygen reduction reaction
PEM : proton exchange membrane
SC : shan and chen

REFERENCES

1. M. M. Mench, *Fuel cell engines,* Wiley, New Jersey (2008).
2. J. Larminie and A. Dicks, *Fuel cell systems explained,* Wiley, England (2003).
3. Y. Wang, K. S. Chen, J. Mishler, S. C. Cho and X. C. Adroher, *Appl. Energy,* **88**, 981 (2011).
4. M. A. Khan, B. Sundén and J. Yuan, *J. Power Sources*, **196**, 7899 (2011).
5. G. H. Song and H. Meng, *Acta Mech. Sin.*, **29**, 318 (2013).
6. H. Ostadi, P. Rama, Y. Liu, R. Chen, X. Zhang and K. Jiang, *Microelectron. Eng.*, **87**, 1640 (2010).
7. M. S. Ismail, K. J. Hughes, D. B. Ingham, L. Ma and M. Pourkashanian, *Appl. Energy*, **95**, 50 (2012).
8. S. Chen and G. D. Doolen, *Annu. Rev. Fluid Mech.*, **30**, 329 (1998).
9. A. S. Joshi, K. N. Grew, A. A. Peracchio and W. K. S. Chiu, *J. Power Sources*, **164**, 631 (2007).
10. J. Park, M. Matsubara and X. Li, *J. Power Sources*, **173**, 404 (2007).
11. M. Aghajani, M. Farhadi and K. Sedighi, *Int. J. Hydrog. Energy*, **35**, 9306 (2010).
12. X. D. Niu, T. Munekata, S. A. Hyodo and K. Suga, *J. Power Sources*, **172**, 542 (2007).
13. J. Park and X. Li, *J. Power Sources*, **178**, 248 (2008).
14. T. Koido, T. Furusawa and K. Moriyama, *J. Power Sources*, **175**, 127 (2008).
15. P. P. Mukherjee, C. Y. Wang and Q. Kang, *Electrochim. Acta*, **54**, 6861 (2009).
16. L. Hao and P. Cheng, *J. Power Sources*, **186**, 104 (2009).
17. L. Hao and P. Cheng, *Int. J. Heat Mass Transfer*, **55**, 133 (2012).
18. L. Hao and P. Cheng, *J. Power Sources*, **195**, 3870 (2010).
19. Y. Ben Salah, Y. Tabe and T. Chikahisa, *J. Power Sources*, **199**, 85 (2012).
20. B. Han, J. Yu and H. Meng, *J. Power Sources*, **202**, 175 (2012).
21. L. Chen, H. B. Luan, Y. L. He, and W. Q. Tao, *Int. J. Therm. Sci.*, **5**, 132 (2012).
22. L. Chen, H. Luan, Y. Feng, C. Song, Y. L. He and W. Q. Tao, *Int. J. Heat Mass Transfer*, **55**, 3834 (2012).
23. L. Chen, Y. L. Feng, C. X. Song, L. Chen, Y. L. He and W. Q. Tao, *Int. J. Heat Mass Transfer*, **63**, 268 (2013).
24. M. C. Sukop and D. T. Thorne, *Lattice Boltzmann modeling, An introduction for geoscientists and engineers,* Springer, Heidelberg (2007).
25. P. L. Bhatnagar, E. P. Gross and M. Krook, *Phys. Rev.,* **94**, 511 (1954).
26. A. A. Mohamad, *Lattice Boltzmann method, fundamentals and engineering applications with computer codes*, Springer, Heidelberg (2011).
27. S. Succi, *The lattice Boltzmann equation for fluid dynamics and beyond numerical mathematics and scientific computation,* Clarendon Press, Oxford (2001).
28. A. K. Gunstensen, D. H. Rothman, S. Zaleski and G. Zanetti, *Phys. Rev. A*, **43**, 4320 (1991).
29. X. Shan and H. Chen, *Phys. Rev. E*, **47**, 1815 (1993).
30. M. R. Swift, W. R. Osborn and J. M. Yeomans, *Phys. Rev. Lett.*, **75**, 830 (1995).
31. X. Shan and G. Doolen, *J. Stat. Phys.*, **81**, 379 (1995).
32. X. Shan and H. Chen, *Phys. Rev. E,* **47**, 3614 (1996).
33. M. R. Kamali, S. Sundaresan, H. E. A. Van den Akker and J. J. J. Gillissen, *Chem. Eng. J.*, **207-208**, 587 (2012).
34. J. H. VanSant, *Conduction heat transfer solutions,* Lawrence Livermore National Laboratory, California (1983).
35. T. V. Nguyen, *J. Electrochem. Soc.*, **143**, 103 (1996).
36. Q. Zou and X. He, *Phys. Fluids*, **9**, 1591 (1997).
37. X. Li, *Principles of fuel cells*, Taylor and Francis Group, New York (2006).
38. A. Parthasarathy, S. Srinivasan, A. J. Appleby and C. R. Martin, *J. Electrochem. Soc.*, **139**, 2530 (1992).
39. T. Berning, D. M. Lu and N. Djilali, *J. Power Sources*, **106**, 284 (2002).
40. W. He, J. S. Yi and T. V. Nguyen, *AIChE J.*, **46**, 2053 (2000).